



Full length article

# Freeze casting of iron oxide subject to a tri-axial nested Helmholtz-coils driven uniform magnetic field for tailored porous scaffolds

Isaac Nelson <sup>a, \*</sup>, Levi Gardner <sup>b</sup>, Krista Carlson <sup>b</sup>, Steven E. Naleway <sup>a</sup><sup>a</sup> Department of Mechanical Engineering, University of Utah, United States<sup>b</sup> Department of Metallurgical Engineering, University of Utah, United States

## ARTICLE INFO

## Article history:

Received 1 February 2019

Received in revised form

1 May 2019

Accepted 1 May 2019

Available online 7 May 2019

## Keywords:

Magnetic freeze casting

Iron oxide

Microstructure alignment

Tri-axial nested Helmholtz coils

## ABSTRACT

In this research, Fe<sub>3</sub>O<sub>4</sub> particles were magnetically manipulated to create porous scaffolds using a tri-axial nested Helmholtz coils-based freeze-casting setup. This novel setup allowed for a uniform magnetic field to be applied in any direction and for it to effectively change directions at any time. Applying a uniform low magnetic field of 7.8 mT in various directions was investigated to fabricate a variety of tailored microstructures and mechanical properties in the resultant scaffolds. It was observed that using the magnetic field aligned up to 81% of the lamellar walls and also altered the area and shape of the pores of the resultant scaffolds. This lamellar wall alignment occurred at every applied magnetic field direction due to the Fe<sub>3</sub>O<sub>4</sub> particles aligning during the freeze-casting process. As a result of this alignment, increases in the mechanical properties of up to 4.1× were observed. The results provide a novel experimental technique for the fabrication of user-defined microstructures in Fe<sub>3</sub>O<sub>4</sub>-based freeze-cast materials that provides significant advantages over previous experimental setups for magnetic freeze casting.

© 2019 Acta Materialia Inc. Published by Elsevier Ltd. All rights reserved.

## 1. Introduction

The freeze casting fabrication process has been heavily researched over the past ~18 years [1–3] due to its ability to create porous ceramic [4–8], polymer [9–13], metal [14–17], and composite structures [18,19]. The process includes four steps: 1) create a colloidal slurry with a freezing solvent (e.g., water) and solid loading particles (e.g., Fe<sub>3</sub>O<sub>4</sub> ceramic particles), 2) directionally freeze the slurry, 3) sublimate the grown ice crystals, and 4) sinter the resultant green body, which results in a porous scaffold. Therefore, the pores in the scaffold are the rough negative of the sublimated ice crystals that shrink to various amounts after particles fuse together from the sintering process [3,4,7,20]. To control the resultant scaffold, various methods have been investigated including altering the slurry constituents [21–25], the freezing rate [26–28] and the freezing direction [29–35], and the use of external force fields (e.g., magnetic, electric, and acoustic) [8,35–40]. These methods of control that occur during one of the first two steps identified above have been defined to be either intrinsic (e.g., altering the slurry constituents or controlling the freezing rate) or

extrinsic control methods (e.g., altering the freezing direction or applying external force fields) [41]. Control of the microstructures and properties of the porous materials created via freeze casting can result in materials with applications in a wide variety of engineering fields such as catalyst supports [42], bone substitutes [6,43–46], dental implants [14,15], and complex composite structures [3,47,48].

The application of magnetic fields during the freeze-casting process is one promising method of extrinsic control [24,37–39]. These fields are applied during the freezing process when the solid loading particles are still suspended in the freezing solvent and, therefore, can be easily manipulated. Previous studies have predominantly been done using permanent magnet setups applied perpendicular to the ice-growth (i.e., freezing) direction and have resulted in an increase of the elastic modulus, E, and ultimate compressive strength, UCS, in this direction [38,39]. Certain permanent magnet setups have resulted in large magnetic field gradients (i.e., non-uniform magnetic fields) that create heterogeneous scaffolds due to particle agglomeration [38], which can be detrimental and lead to unintended stress concentrations in the scaffolds. Because of the size of commercially available permanent magnetics, it is difficult to create a uniform magnetic field in a volume the size of a typical freeze-casting slurry.

In addition to particle agglomeration, the use of permanent

\* Corresponding author.

E-mail address: [u1106102@utah.edu](mailto:u1106102@utah.edu) (I. Nelson).

magnets for magnetic freeze casting has required that additional experimental designs and instrumentation be fabricated to apply a diverse set of fields (i.e., magnetic fields parallel, radial, or transverse to the ice-growth direction need to have completely different experimental setups) [40]. While there have been reports on the use of rotating fields created through permanent magnet setups [38], these are difficult to adjust to create dynamically complex fields. If the desire is to control the magnetic field direction and magnitude throughout the freezing process, then using permanent magnets limit this ability.

A good solution to solve these issues of a non-uniform magnetic field and the inability to apply a magnetic field in any direction is the use of tri-axial nested Helmholtz coils. Theoretical modeling has predicted that a single Helmholtz coil has drastically lower magnetic field gradient error when compared to common permanent magnet freeze-casting setups, with <1% and 109%, respectively [39]. Thus the Helmholtz coil is capable of creating a near-uniform magnetic field. By nesting three Helmholtz coils in mutually orthogonal directions to create tri-axial nested Helmholtz coils, it has also been demonstrated previously (though not in freeze casting) that this near-uniform field can be applied in any direction [49].

If particles are not responsive to the applied magnetic field, they won't align and interact in a manner desirable to magnetic freeze casting. To successfully get particles to align, the interaction energy between particles needs to be high enough through their magnetic properties (i.e., their magnetic moments). This interaction can be accomplished by using particles with inherently high magnetization, such as ferrimagnetic particles (e.g.,  $\text{Fe}_3\text{O}_4$ ) [39], increasing the applied magnetic field up until magnetic saturation occurs, or both. Additionally, creating superparamagnetic (inherently high magnetization) particle coated diamagnetic (inherently low magnetization) particles for magnetic freeze casting has been done to get particles to interact under the magnetic field conditions [37], however, these coated particles still tend to have lower magnetizations than ferrimagnetic particles.

Depending on the application of the final fabricated material, the desire might be to have either a high or low magnetic properties. For example, having high magnetic properties can be desirable in applications such as motors, robotic materials, and for the separation of non-magnetic and magnetic materials. However, in applications such as bone substitutes, dental implants, and certain electrical components, it is desirable to have very low magnetic properties. To understand how the magnetic properties of the  $\text{Fe}_3\text{O}_4$  scaffolds change in the following fabrication process, experiments to characterize the magnetic properties were performed.

In this research, an understanding of how the microstructure and mechanical properties change as a result of applying a uniform magnetic field via tri-axial nested Helmholtz coils in various directions while resulting in materials with low magnetic susceptibility was investigated. With the ability to apply a magnetic field in any direction, this research expands on previous work where applying a magnetic field parallel [39], and perpendicular [24,36–38,40] to the ice growth direction was investigated. For each magnetic field direction applied, mechanical tests were done in multiple directions to gain an understanding of how applying a magnetic field alters the mechanical properties in these various directions. This research aims to characterize the operating domain of magnetic freeze casting actuated by a tri-axial nested Helmholtz coils.

## 2. Materials and methods

### 2.1. Tri-axial nested Helmholtz coils-based magnetic freeze casting setup and validation

Expanding on a previously employed uniaxial Helmholtz coil-

based freeze casting setup [39], a tri-axial nested Helmholtz coils-based freeze casting setup was fabricated for this research. These nested Helmholtz coils were designed and constructed based on steps described in detail by Abbott [49] and are illustrated and photographed in Fig. 1. A Helmholtz coil is a pair of same-sized solenoids connect in series and aligned coaxially where the distance between two solenoids is equal to the radius of the solenoids. The tri-axial nested Helmholtz-coils setup consists of three mutually orthogonal Helmholtz coils nested within each other. The small coil creates a magnetic field in the y-direction, the medium coil a magnetic field in the x-direction, and the large coil a magnetic field in the z-direction (as defined in Fig. 1). By controlling the current through each Helmholtz coil, a magnetic field can be created in any desired direction.

A comparison between the theoretical and experimental values of the coil current it takes to generate a 7.8 mT magnetic field via the tri-axial nested Helmholtz coils was performed. This magnetic field is incrementally higher than low magnetic fields used in a previous study of 2.6 and 5.2 mT [39], allowing for future comparisons. This was done to observe the error associated with the construction of the coils. For a Helmholtz coil, the magnetic field generated at the center of the workspace is theoretically given by Abbott [49]:

$$B = \frac{1.43J\epsilon(X_c - \delta_0)^2\mu_0}{D_c} \quad (1)$$

where  $J$  is the current density:

$$J = \frac{I}{\frac{\pi}{4}d_i^2} \quad (2)$$

$\epsilon$  is the packing efficiency:

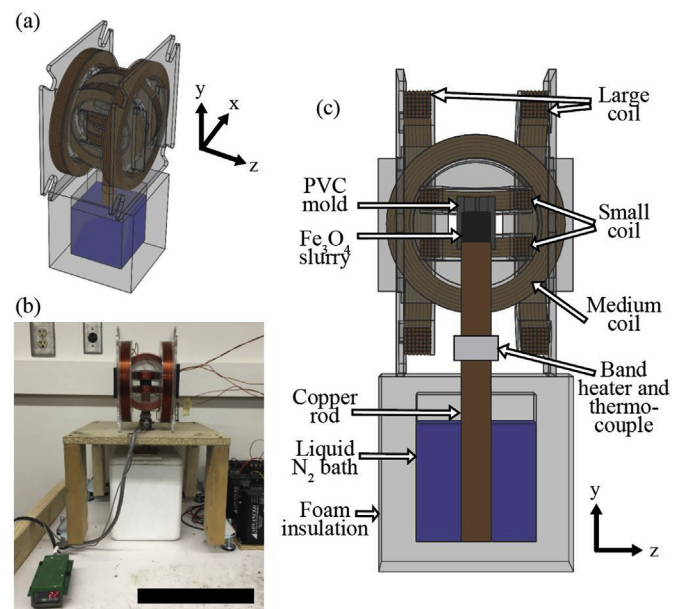


**Fig. 1.** (a) An illustrated trimetric view of the magnetic freeze casting setup. (b) A picture of the experimental setup used in this research. The scale bar is 30 cm. (c) A y-z cross-section illustrated view indicating each of the nested three nested coils aligned with the center of the  $\text{Fe}_3\text{O}_4$  slurry.

$$\varepsilon = \frac{\pi \delta_o^2}{2\sqrt{3}\delta_i^2} \quad (3)$$

$X_c$  is the length of a side of the square cross section of a solenoid,  $\delta_o$  is the diameter outside of the insulated circular magnetic wire,  $\delta_i$  is the diameter inside of the insulation of the insulated circular magnetic wire,  $\mu_o$  is the permeability of free space,  $D_c$  is the diameter of the coil, and  $I$  is the coil current. With Equations (1)–(3), solving for  $I$  gives:

$$I = \frac{\pi B D_c \delta_i^2}{5.72 \varepsilon (X_c - \delta_o)^2 \mu_o} \quad (4)$$

To experimentally measure the coil current, a multimeter was connected in parallel to each coil. Using Equation (4) as the theoretical coil current value, the percent error between the theoretical and experimental coil current values is calculated by:

$$\% \text{ error} = \frac{I_{\text{theoretical}} - I_{\text{experimental}}}{I_{\text{theoretical}}} \cdot 100 \quad (5)$$

To experimentally validate that the magnetic field can align particles in each direction, 0.05 g of  $\text{Fe}_3\text{O}_4$  particles of ~200 nm diameter from ACROS Organics (Pittsburgh, PA, USA) were poured into a clear 21 mm inner diameter plastic cylinder containing 1 mL of water. This cylinder was then placed at the center of the tri-axial nested Helmholtz coils. A magnetic field of 7.8 mT was applied in the z-direction, x-direction, y-direction, and the x- and y-medial direction (i.e., 45°-direction) to observe if, under these conditions, the particles aligned in the direction of the applied magnetic field. Also, the magnetic field was applied in the x-direction and was then changed to the z-direction to observe the time required to realign particles under a dynamic field.

## 2.2. Sample preparation

To create the freeze-casting slurries,  $\text{Fe}_3\text{O}_4$  (with a particle size of ~200 nm) from ACROS Organics (Pittsburgh, PA, USA) was used as the solid loading particles, polyethylene glycol of  $10,000 \text{ g mol}^{-1}$  and polyvinyl alcohol of  $88,000\text{--}97,000 \text{ g mol}^{-1}$  from Alfa Aesar (Ward Hill, MA, USA) were used as polymeric binders, Darvan 811 of  $3500 \text{ g mol}^{-1}$  from R. T. Vanderbilt Company, Inc. (Norwalk, CT, USA) was used as a dispersant, and tap water was used as the freezing solvent. For each scaffold, an 8 mL slurry of 10 vol%  $\text{Fe}_3\text{O}_4$  and 1 vol% of polyethylene glycol, polyvinyl alcohol and Darvan 811 were sonicated at 42 kHz for 12 min in a 40 mL plastic bag to create a colloid. Note that this technique has previously proven successful at creating colloids for freeze casting [50,51]. Immediately following the sonication, the slurry was poured into the PVC mold shown in Fig. 1c. Once in the PVC mold, the slurry was subject to no magnetic field (as a baseline), or a magnetic field from the tri-axial nested Helmholtz coils while being directionally frozen at  $10^\circ \text{C min}^{-1}$  in the y-direction.

A total of 60 slurries were fabricated into scaffolds with 10 being fabricated under no magnetic field (i.e., 0 mT), and 10 each being fabricated under one of five different magnetic field configurations described below:

- **Single Direction Magnetic Field:** freezing a slurry subject to a magnetic field of 7.8 mT in the z-direction, x-direction, y-direction, and the 45°-direction as shown in Fig. 2.
- **Multi-Direction Magnetic Field:** freezing a slurry while changing the 7.8 mT magnetic field from the x-to the z-direction about halfway through the slurry freezing as shown in Fig. 3. To

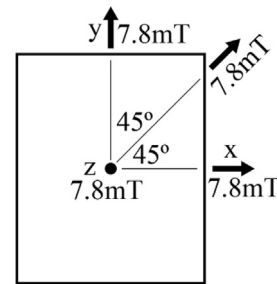


Fig. 2. Slurries were subject to no magnetic field (i.e., 0 mT) and four single-direction magnetic fields during freezing: 1) 7.8 mT in the z-direction, 2) 7.8 mT in the x-direction, 3) 7.8 mT in the y-direction and 4) 7.8 mT in the 45°-direction. Directions are presented on a representative surface that portrays an x-y cross-section of the center of the slurry.

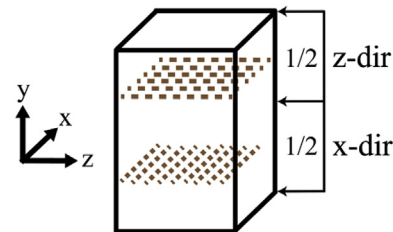


Fig. 3. Slurries were subject to a 7.8 mT magnetic field in the x-direction and flipped to the z-direction halfway through the freezing process. Directions are presented on a representative volume that portrays the center of the slurry.

approximate the halfway point of the slurry, the magnetic field was changed from the x-to the z-direction after 8.5 min of freezing. This time was chosen as half of the time empirically observed for a  $\text{Fe}_3\text{O}_4$  8 mL slurries to freeze fully.

All slurries were frozen at a magnetic field strength of 7.8 mT. Following the freezing process, the slurries were lyophilized at 0.047 mBar and  $-51^\circ \text{C}$  for 72 h in a Labconco FreeZone 1 freeze drier (Kansas City, MO, USA) to sublimate the grown ice crystals. The green bodies were next sintered at  $1150^\circ \text{C}$  for 20 min, with a heating and cooling rate of  $2^\circ \text{C min}^{-1}$  in an open-air Keith KSK-12 1700 furnace (Pico Rivera, CA, USA).

## 2.3. Crystallographic characterization

To determine the crystallographic changes from the sintering process, powder X-ray diffraction (PXRD) of iron oxide samples (created using the  $\text{Fe}_3\text{O}_4$ -based freeze-casting process described above) were performed using a Miniflex600 diffractometer (Rigaku Corporation, Tokyo, Japan). Scans were run over a range of  $10\text{--}80^\circ 2\theta$  at a rate of  $0.5^\circ 2\theta \text{ min}^{-1}$  and a step size of  $0.05^\circ 2\theta$ . Particles were prepared by crushing sintered scaffold samples and sieving to a particle size range of less than  $53 \mu\text{m}$ . The as-received particles, particles after the full sintering cycle, and particles sintered to an intermediate cycle of  $400^\circ \text{C}$  at a heating and cooling rate of  $2^\circ \text{C min}^{-1}$  were characterized.

## 2.4. Magnetic characteristics

Because the control of the ferrimagnetic  $\text{Fe}_3\text{O}_4$  particles is dependent on its magnetic properties and that  $\text{Fe}_3\text{O}_4$  is well known to oxidize when sintered in the air  $400^\circ \text{C}$  [52], the magnetic properties as a function of sintering were observed. To do this, magnetization curves were generated using a Microsense FCM-10

vibrating-sample magnetometer (Lowell, MA, USA) on particles that were prepared by crushing sintered scaffold samples and sieving to a particle size range of less than 53  $\mu\text{m}$ . The mass of the as-received particles, particles after the full sintering cycle, and particles sintered to an intermediate cycle were measured prior to testing to get their mass magnetization.

## 2.5. Structural characterization

The scaffold microstructure was imaged using an FEI Quanta 600 FG (Hillsboro, Oregon, USA) scanning electron microscope (SEM). Eight x-z plane (perpendicular to the ice growth) SEM images at an acceleration voltage of 5 kV and spot size of 3 nm were taken 4 mm from the top of each scaffold and eight images 4 mm from the bottom of each scaffold to measure the porosity, pore area, major axis length, minor axis length and pore aspect ratio (i.e., major axis/minor axis). For each image, these measurements were made using ImageJ software (National Institutes of Health, Bethesda, MD, USA) by adjusting the threshold similar to methods used in previous studies [37,38].

To further quantify how the microstructure changed as a result of the magnetic field direction, the x-z plane SEM images were also used to observe the lamellar wall direction. This was done by defining four ranges of angles, in a manner similar to a previous report [24]. These ranges are  $0^\circ \pm 22.5^\circ$ ,  $45^\circ \pm 22.5^\circ$ ,  $90^\circ \pm 22.5^\circ$ , and  $135^\circ \pm 22.5^\circ$  where  $0^\circ$  is in the x-direction, and  $90^\circ$  is in the z-direction as shown in Fig. 4a. In freeze-cast scaffolds, there are areas where the lamellar walls are all in a specific direction [4]. As shown in an example in Fig. 4b, these areas and lamellar wall angles were measured across each SEM image using ImageJ. For each scaffold, the percent area of lamellar walls in each of the four defined ranges was calculated using the following equation:

$$\% \text{ area in angle range } n = \frac{\text{total imaged scaffold surface area in angle range } n}{\text{total imaged surface area in scaffold}} \cdot 100 \quad (6)$$

For the example shown in Fig. 4b, the image has a total surface area of  $189872 \mu\text{m}^2$  with a surface area of  $116817 \mu\text{m}^2$  with lamellar walls at  $18^\circ$  making it in the  $0^\circ \pm 22.5^\circ$  range and  $73055 \mu\text{m}^2$  with lamellar walls at  $114^\circ$  making it in the  $135^\circ \pm 22.5^\circ$  range. The surface areas measured in this image were 1 of the 16 images taken of the scaffold where the percent areas for each range of angles were calculated using Equation (6) for each scaffold.

SEM images in the x-y plane (parallel to the ice growth) were taken to measure the lamellar wall direction in this plane. Twelve angle measurements of the lamellar walls were taken across the x-axis of each scaffold using ImageJ. As the lamellar walls will naturally be directed by the ice-growth, the y-direction (i.e., ice-growth direction) is considered to be  $0^\circ$  and clockwise towards the x-direction is defined as positive and counterclockwise is defined as negative as shown in Fig. 4c. An example is shown in Fig. 4d where an angle of  $-2^\circ$  is measured. Additionally, for the multi-directional magnetic field scaffolds, SEM images at the location where the magnetic field direction changed were taken to observe the interface.

## 2.6. Mechanical characterization

For each scaffold, four rectangular shaped samples where the initial heights were approximately 5 mm and the cross-sectional

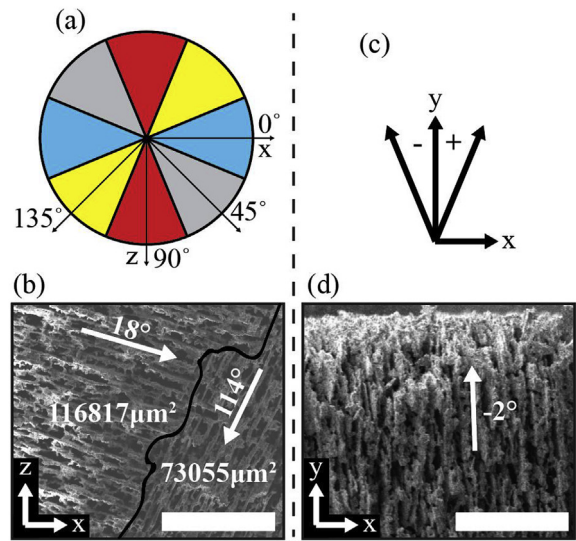


Fig. 4. (a) The four defined ranges of angles in the x-z plane where  $0^\circ$  is in the x-direction and  $90^\circ$  is in the z-direction. (b) An SEM image example of areas associated with a lamellar wall direction and the calculated area and angle in the x-z plane. (c) The defined positive and negative directions of the lamellar walls in the x-y plane. (d) An SEM image example of the lamellar wall direction in the x-y plane. The scale bars are all 200  $\mu\text{m}$ .

areas were approximately  $60 \text{ mm}^2$  were cut from the midsection (i.e., homogenous lamellar ice-growth region [53,54]) to perform compression tests. Of the four samples, two were compressed in the y-direction and two in the x-direction using an Instron 5967 load frame with an Instron 30 kN load cell (Norwood, MA, USA) at a

controlled crosshead speed of  $1 \text{ mm min}^{-1}$ . This results in 20 compression tests for each magnetic field configuration in each direction. The ultimate compressive strength ( $\text{UCS}_y$  and  $\text{UCS}_x$ ) was recorded as the engineering compression stress at the elastic limit, and the elastic modulus ( $E_y$  and  $E_x$ ) was recorded as the slope of the linear elastic region observed in the stress-strain curve. The scaffolds were compressed to 0.1 strain to observe the failure after the UCS.

## 2.7. Statistical analysis

For every measured property:  $\text{UCS}_y$ ,  $\text{UCS}_x$ ,  $E_y$ ,  $E_x$ , porosity, pore area, major axis, minor axis, and lamellar wall direction, a one-way analysis of variance (ANOVA) was performed using MATLAB software (Natick, MA, USA) based on the fixed-treatment factor *magnetic field direction* and a significant difference of  $\alpha = 0.05$ . If the one-way ANOVA result found that there was a statistically significant difference, this meant that there was a highly likely probability ( $\geq 95\%$ ) that the properties were affected by the magnetic field direction. Following the ANOVA test, a Tukey's honest significant difference (HSD) test was performed ( $\alpha = 0.05$ ). This test makes a pairwise comparison across each direction of the magnetic field to pinpoint which scaffolds displayed statistically significant differences from each other. This statistical method has been used previously in freeze cast research [8,21].

### 3. Results

#### 3.1. Experimental setup validation

The theoretical coil current from Equation (4), the experimental coil current, and the % error from Equation (5) when generating 7.8 mT for each Helmholtz coil is shown in Table 1. Theoretical values were measured from the experimental setup to be  $X_c = 17.77$ , 20.25, and 23.875 mm, and  $D_c = 78.25$ , 131, and 199 mm, for the small, medium and large coils respectively. For all the coils, theoretical values of  $\delta_o = 1.7145$  mm,  $\delta_i = 1.6281$  mm,  $B = 7.8$  mT, and  $\mu_o = 4\pi \cdot 10^{-7}$  T m A<sup>-1</sup> were used. The values reported are at the center of the workspace (i.e., the center of the slurry). Because the magnetic field in the slurry volume is near uniform [39] and the center is the target magnetic field, only this location was necessary to compare the coil current values. While the measured errors are quite small and care was taken to minimize construction error, there are several areas where inherent variability could be present in the experimental setup. Specifically, the solenoids not being perfectly coaxial and dimensionally identical, the wire packing efficiency not being as precise as theoretical, and minor variations in wire diameter as reported by the manufacturer. The experimental coil currents were applied to the coils in order to ensure a 7.8 mT magnetic field throughout this work.

To ensure that the tri-axial nested Helmholtz-coils setup was capable of accurately aligning particles in any direction without causing particle agglomeration, a simple water and Fe<sub>3</sub>O<sub>4</sub>-particle mixture was controlled in the same orientations that are tested throughout this research. This water and Fe<sub>3</sub>O<sub>4</sub> mixture was used because the freeze-cast slurries were opaque and not capable of being optically imaged due to the Fe<sub>3</sub>O<sub>4</sub> vol% and added binders. The Fe<sub>3</sub>O<sub>4</sub> particles aligned with the direction of the applied 7.8 mT magnetic field. As shown in the optical images in Fig. 5, alignment was qualitatively demonstrated in the, z-, x-, y- and 45°-directions. The uniformity of the magnetic field, which has been experimentally demonstrated and modeled in previous work [39], was also qualitatively observed as the particles did not agglomerate or migrate towards the solenoids. The applied current in the setup can be changed within microseconds [55], with the Fe<sub>3</sub>O<sub>4</sub> particles realigning within less than a second (Supplemental Video 1). Therefore, when working with the multi-direction magnetic fields in this work, the slurry was expected to react within a very small amount of time (<1 s).

Supplementary video related to this article can be found at <https://doi.org/10.1016/j.actamat.2019.05.003>

#### 3.2. PXRD and magnetic characteristics

Fig. 6a shows the PXRD data for different iron oxide species produced before sintering, at the intermediate cycle of 400 °C, and after the full sintering cycle of 1150 °C. The changes in particle color are shown in Fig. 6b. The original black colored feedstock particles match cubic Fe<sub>3</sub>O<sub>4</sub> (ICDD PDF Card 01-086-1358). After the full sintering cycle, a structural transition matching rhombohedral  $\alpha$ -Fe<sub>2</sub>O<sub>3</sub> (ICDD PDF Card 01-076-9683) with a dark grey coloring observed. The Fe<sub>3</sub>O<sub>4</sub> samples heated to the intermediate cycle

exhibited a structure matching  $\gamma$ -Fe<sub>2</sub>O<sub>3</sub> (ICDD PDF Card 01-089-5892) and a red color. Steady-state Fe<sub>3</sub>O<sub>4</sub> oxidation was shown to be a diffusion-controlled mechanism [56–58]. Therefore, the prolonged heating below 1450 °C resulted in a transition to Fe<sub>2</sub>O<sub>3</sub> [59].

The iron oxide crystallographic changes resulted in magnetic property changes. The as-received Fe<sub>3</sub>O<sub>4</sub> particles exhibited ferromagnetic properties in the magnetization curve shown in Fig. 6c. When the particles changed to  $\gamma$ -Fe<sub>2</sub>O<sub>3</sub> at 400 °C, they also exhibited ferromagnetic properties, though with a lower saturation magnetization. After the sintering process, the particles changed to  $\alpha$ -Fe<sub>2</sub>O<sub>3</sub> and exhibited weak ferromagnetic properties. Therefore, while the particles employed during freeze casting were ferromagnetic, the sintering process greatly reduces the particle's magnetizations and resulted in a final scaffold with much lower magnetization, which may be beneficial for certain applications. If it is desired to have higher greater magnetic properties in the resultant scaffolds, one way is to sinter Fe<sub>3</sub>O<sub>4</sub> in an inert argon gas environment [39,52].

#### 3.3. Single direction magnetic field structural properties

The microstructural properties of porosity, pore area, major axis, minor axis, and pore aspect ratio are shown in Table 2. It was observed that the pore area increased by 8.9% and 7.9% when applying a magnetic field in the z- and x-direction (i.e., perpendicular to the ice-growth direction) respectively compared to 0 mT. The major axis and pore aspect ratio increased, while the minor axis decreased, all by statistically significant amounts when applying 0 mT compared to applying the magnetic field in the z- and x-direction (Table 2). These increases are attributed to the Fe<sub>3</sub>O<sub>4</sub> particles aligning perpendicular to the ice-growth direction, thus making it more energetically favorable for the particles to be rejected and not entrapped by the freezing front creating longer pores with higher aspect ratios. When rejected by the freezing front, the particles become part of the lamellar walls, when entrapped by the freezing front, the particles become mineral bridges thus creating smaller pores [5,41]. Although there was a decrease in the mean porosity when applying the magnetic field in the y-direction which is due to the lamellar walls being more aligned in the y-direction, as was previously observed [39], it did not result in a statistically significant difference. This is hypothesized to be due to the difference in the sintering procedures.

The lamellar walls were observed to align in the direction of the applied magnetic field in the x-z plane. When applying 0 mT, the lamellar wall directions were fairly evenly distributed resulting in no statistically significant differences across all four ranges of directions as shown in Fig. 7a. In the SEM image in Fig. 7b, it was apparent that the lamellar walls do not align in any specific direction. When applying 7.8 mT in the z-direction, 81% of the lamellar walls aligned in the 90°±22.5° range of angles (Fig. 7c). This range of angles was in the z-direction and was statistically significantly different from all other ranges of angles, indicating that when applying a magnetic field in the z-direction, most of the lamellar walls will align in that direction (a representative SEM image is shown in Fig. 7d). When applying 7.8 mT in the x-direction, 80% of the lamellar walls aligned in the 0°±22.5° range of angles (Fig. 7e). Again, it was observed that this range of angles was statistically significantly different from all other ranges of angles, indicating that when a magnetic field in the x-direction, most of the lamellar walls will align in that direction (a representative SEM image is shown in Fig. 7f). This lamellar wall alignment transverse to the ice-growth direction (i.e., x- and z-direction) has been observed previously when applying magnetic fields driven by permanent magnets in these directions [37,38]. Similar to the case of applying 0 mT, no statistically significant differences occurred

**Table 1**

The theoretical coil current from Equation (4), the experimental coil current, and the % error from Equation (5) when generating 7.8 mT for each Helmholtz coil.

Helmholtz coil	Theoretical (A)	Experimental (A)	Error (%)
Small	3.36	3.11	7.51
Medium	4.21	4.06	3.64
Large	4.48	4.38	1.51

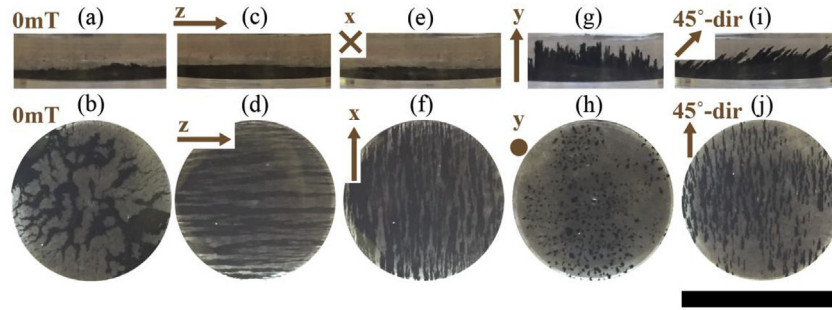


**Fig. 5.** Optical images of  $\text{Fe}_3\text{O}_4$  particles when applying 0 mT viewed in the (a) y-z plane and (b) x-z plane and applying 7.8 mT in the z-direction viewed in the (c) y-z plane and (d) x-z plane, in the x-direction viewed in the (e) y-z plane and (f) x-z plane, in the y-direction viewed in the (g) y-z plane and (h) x-z plane, and in the 45°-direction viewed in the (i) x-y plane and (j) x-z plane. Note, 'X' in (e) is defined as the direction into the page, and '●' in (g) is defined as the direction out of the page. The scale bar is 20 mm.

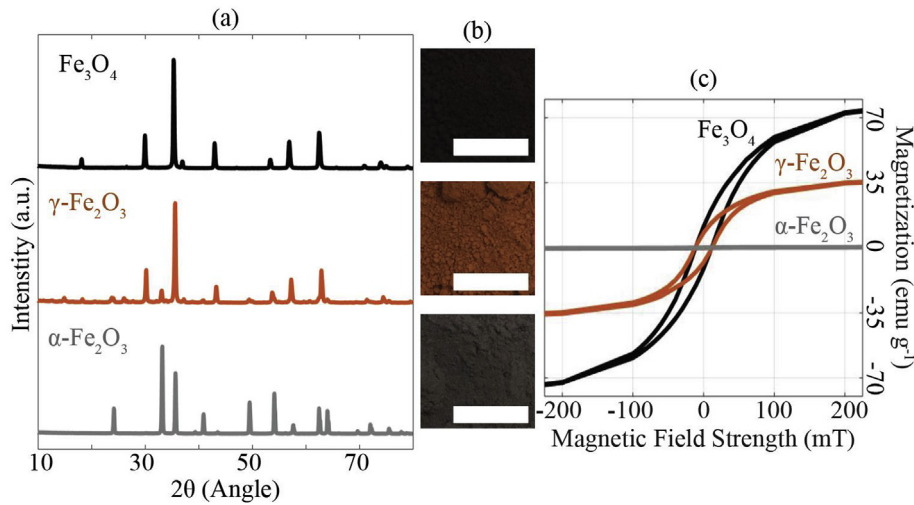


**Fig. 6.** (a) The PXRD spectra of as-received  $\text{Fe}_3\text{O}_4$  particles (ICDD PDF Card 01-086-1358),  $\gamma\text{-Fe}_2\text{O}_3$  particles (ICDD PDF Card 01-089-5892) sintered to the intermediate cycle of 400 °C and  $\alpha\text{-Fe}_2\text{O}_3$  particles (ICDD PDF Card 01-076-9683) to the full sintering cycle of 1150 °C. (b) The change in color of the particles can be noticed for each case. The scale bars are all 8 mm. (c) The magnetization curves for each particle showing a decline in the magnetization with effectively no magnetization for the  $\alpha\text{-Fe}_2\text{O}_3$  material. (For interpretation of the references to color in this figure legend, the reader is referred to the Web version of this article.)

**Table 2**

The structural properties, reported as a mean  $\pm$  one standard deviation of  $n \approx 10,000$  measurements of scaffolds fabricated while applying no magnetic field (0 mT) and 7.8 mT in the z-direction, x-direction, y-direction, and between the x- and y-direction (45°). All observed properties found to have statistically significant differences ( $\alpha = 0.05$ ) are noted by matching letters a-i.

Magnetic Field Direction	Area Porosity (%)	Pore Area ( $\mu\text{m}^2$ )	Major Axis ( $\mu\text{m}$ )	Minor Axis ( $\mu\text{m}$ )	Pore Aspect Ratio
0 mT	23.2 $\pm$ 2.5	303 $\pm$ 199 <sub>a,b</sub>	32.0 $\pm$ 13.3 <sub>a,b,c</sub>	11.8 $\pm$ 3.7 <sub>a,b,c</sub>	2.9 $\pm$ 1.4 <sub>a,b,c</sub>
z	21.9 $\pm$ 2.6	330 $\pm$ 247 <sub>a,c,d</sub>	38.2 $\pm$ 17.8 <sub>a,d,e,f</sub>	10.7 $\pm$ 3.4 <sub>a,d,e,f</sub>	3.7 $\pm$ 1.8 <sub>a,d,e,f</sub>
x	20.3 $\pm$ 4.1	327 $\pm$ 224 <sub>b,e,f</sub>	36.3 $\pm$ 17.0 <sub>b,d,g,h</sub>	11.3 $\pm$ 3.5 <sub>b,d,g,h</sub>	3.5 $\pm$ 1.8 <sub>b,d,g,h</sub>
y	20.5 $\pm$ 3.3	299 $\pm$ 199 <sub>f,d</sub>	30.7 $\pm$ 12.3 <sub>c,e,g</sub>	12.1 $\pm$ 3.7 <sub>c,e,g,i</sub>	2.8 $\pm$ 1.3 <sub>c,e,g,i</sub>
45°	18.9 $\pm$ 1.8	302 $\pm$ 187 <sub>c,e</sub>	31.6 $\pm$ 12.8 <sub>f,h</sub>	12.0 $\pm$ 3.6 <sub>f,h,i</sub>	2.9 $\pm$ 1.4 <sub>f,h,i</sub>

when applying a 7.8 mT magnetic field in the y-direction (Fig. 7g) indicating that the lamellar walls do not align in any specific direction (as shown in the representative SEM image in Fig. 7h) in the x-z plane. When applying 7.8 mT in the 45°-direction, 53% of the lamellar walls aligned in the  $0^\circ \pm 22.5^\circ$  range of angles (Fig. 7i). At this 45°-direction there was an x- and y-direction component to the magnetic field vector of about 5.5 mT (from  $7.8 \text{ mT} \cdot \cos 45^\circ$ ). The x-direction component is what contributes to the lamellar walls being more aligned in the  $0^\circ \pm 22.5^\circ$  range of angles than any other. There was a statistically significant difference between this range of angles and the others indicating that applying a magnetic field at this 45°-direction results in lamellar walls favoring to align in the x-direction (a representative SEM image is shown in Fig. 7j).

The lamellar wall directions in the x-y direction (Fig. 4c) for each applied magnetic field direction are shown in the box-and-whisker plot in Fig. 7k. A box-and-whisker plot was used to observe the distribution of the measured lamellar wall directions because the means are all close to zero (excluding the 45°-direction), as the majority of lamellar walls align with the y-direction, which was also the ice-growth direction. The range of the lamellar wall angles (i.e., from whisker to whisker) was as high as 39° and as low as 15° when applying 0 mT and the magnetic field in the y-direction respectively. More lamellar walls were near the y-direction (i.e.,  $0^\circ$ ) when applying the magnetic field in the y-direction because the magnetic field made it favorable for the particles to align in this direction. The median lamellar wall angle when applying the magnetic field in the

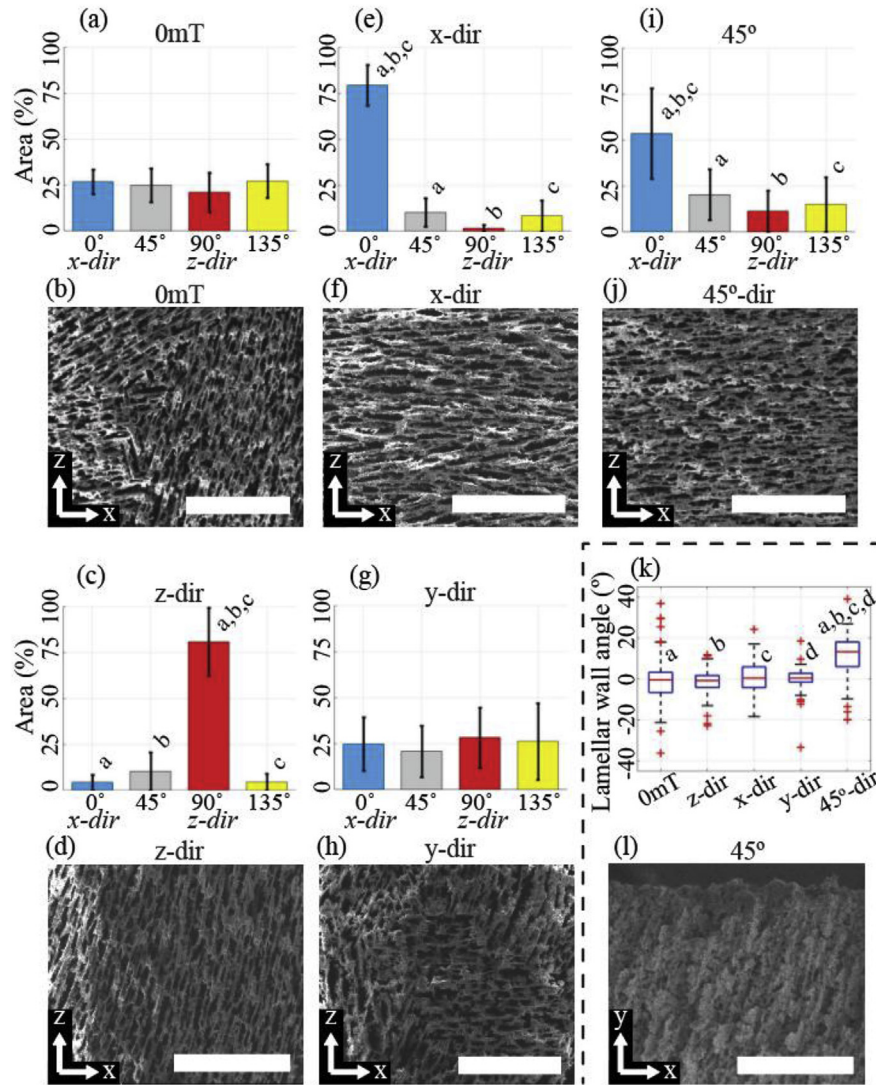


**Fig. 7.** The percent area in angle ranges  $0^\circ \pm 22.5^\circ$ ,  $45^\circ \pm 22.5^\circ$ ,  $90^\circ \pm 22.5^\circ$ , and  $135^\circ \pm 22.5^\circ$  (see Fig. 4a) and a representative SEM image to observe the lamellar wall directions when applying (a, b) 0 mT, and 7.8 mT in the (c, d) z-direction, (e, f) x-direction, (g, h) y-direction, and (i, j) 45°-direction (i.e. between the x- and y-directions). (k) A box-and-whisker plot of the measured lamellar wall directions in the x-y plane for each single-direction magnetic field and (l) an x-y plane SEM image when the magnetic field was applied in the 45°-direction. The '+' in the box-and-whisker plot are outlier points. All observed properties found to have statistically significant differences ( $\alpha = 0.05$ ) are noted by matching letters a-d. The scale bars are all 200  $\mu\text{m}$ .

45°-direction was  $13^\circ$  suggesting that the magnetic field makes the lamellar walls align away from the y-direction and towards the magnetic field direction as shown in Fig. 7. It was theorized that the walls are at an angle of  $13^\circ$  (as opposed to  $45^\circ$ ) due to the competing forces of the ice-growth (in the y-direction) and the magnetic field ( $45^\circ$  from the y-direction), though further investigation of the specific physical interaction between these forces was beyond the scope of this research. A statistically significant difference between the 45°-direction and all other directions occurred, thus demonstrating that applying a field angled away from the ice-growth direction can significantly alter the orientation of the lamellar walls.

### 3.4. Single direction magnetic field mechanical properties

The mechanical properties for the single-direction scaffolds are shown in Fig. 8. The  $UCS_x$  was greatest when applying a magnetic field in the x-direction as shown in Fig. 8a. An increase of 142%, 262%, 111%, and 39% was observed when comparing applying the

magnetic field in the x-direction to 0 mT, the z-direction, y-direction, and the 45°-direction, respectively. Applying the magnetic field in the x-direction resulted in statistically significant differences to every other magnetic field direction. This was due to the lamellar walls aligning (Fig. 7e) in the compression direction. The second strongest applied magnetic field direction was the 45°-direction and the increase of 160% and statistically significant difference between applying a magnetic field in the z-direction compared to the 45°-direction (Fig. 8a) was attributed to the majority of the lamellar walls being aligned either perpendicular (for the z-direction, Fig. 7c) or aligned parallel (for the 45°-direction, Fig. 7i) to the compression direction, respectively. It was hypothesized that between applying 0 mT and a magnetic field in the z-direction would result in a lower  $UCS_x$  because more lamellar walls were aligned perpendicular (Fig. 7c) to the direction of compression. However, the observed decrease between the means of 50% did not result in a statistically significant difference.

The  $E_x$  compression tests resulted in statistically significant differences between applying a magnetic field in the x-direction to

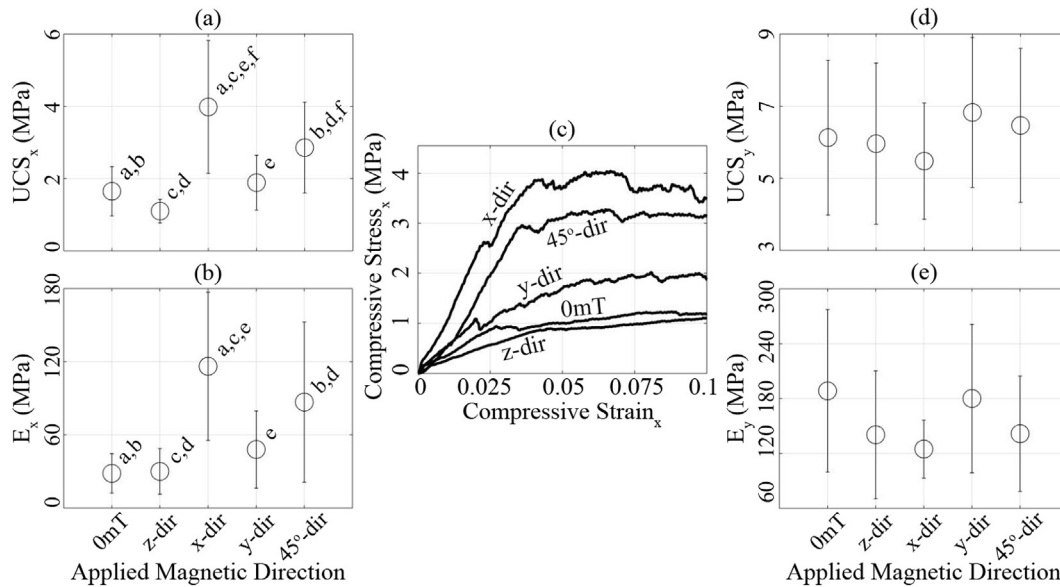


**Fig. 8.** The (a) UCS<sub>x</sub> and (b) E<sub>x</sub> of scaffolds fabricated with the application of a single direction magnetic field. (c) Stress-strain curves showing the variable responses of x-direction compression tests on scaffolds fabricated with the magnetic field applied at each direction. After the UCS<sub>x</sub> is reached, the scaffolds sustain loading due to their cellular nature. The (d) UCS<sub>y</sub> and (e) E<sub>y</sub> of scaffolds fabricated with the application of a single direction magnetic field. The values shown are the means ± one standard deviation. All observed properties found to have statistically significant differences ( $\alpha = 0.05$ ) are noted by matching letters a-f.

every other direction as shown in Fig. 8b. An increase of 308%, 286%, 142%, and 34% occurred when comparing applying the magnetic field in the x-direction to 0 mT, the z-direction, y-direction, and the 45°-direction respectively. Additionally, statistically significant differences were observed between applying a magnetic field in the 45°-direction compared to 0 mT and the z-direction. An increase of 205% and 189% occurred when comparing applying the magnetic field in the 45°-direction to 0 mT and the z-direction respectively. Similar to the UCS<sub>x</sub> results, the E<sub>x</sub> results are due to the alignment of the lamellar wall direction being controlled by the direction of the applied magnetic field. To illustrate the full stress-strain response of the x-direction compression tests, Fig. 8c shows a curve for a scaffold fabricated with the magnetic field applied at each direction. It was observed that following the UCS<sub>x</sub>, the stress was sustained due to the cellular nature of the scaffolds.

Previous reports proposed that a decrease in the pore area and pore aspect ratio would result in the increase of the UCS<sub>y</sub> and E<sub>y</sub> by delaying lamellar buckling [28,60]. However, this does not occur in the results shown in Fig. 8d and e. Of note, the magnetic properties in the resultant scaffolds (Fig. 6) resulted in lower magnitudes of UCS<sub>y</sub> and E<sub>y</sub>. This was in contrast with using an inert gas sintering process that results in higher UCS<sub>y</sub> and E<sub>y</sub> scaffolds but with the downside of higher magnetic property scaffolds [39].

### 3.5. Multi-direction magnetic field structural properties

The uniqueness of this tri-axial nested Helmholtz-coils-based setup allows for the magnetic field to be applied in any direction and for that direction to be changed at any time (as demonstrated in Section 3.1). To demonstrate this in freeze-cast scaffolds, this capability was successfully used to change the magnetic field from the x-to the z-direction about halfway through freezing the slurry. Functionally, it was accomplished by applying the appropriate coil current (4.22 A) through the medium coil, then reducing this current to 0 A and applying a coil current (4.48 A) to the large coil to produce a magnetic field of 7.8 mT in each direction.

The microstructural properties observed when changing the 7.8 mT direction from the x-direction to the z-direction halfway

through the slurry freezing are shown in Table 3. For most of the microstructural properties (i.e., porosity, pore area, and minor axis), no statistically significant differences between the top (z-direction) and bottom (x-direction) of the scaffold were observed. The two exceptions were the major axis and the pore aspect ratio (which inherently depends on the major axis). A statistically significant difference was not found when comparing the multi-direction magnetic field properties (i.e., z-direction and x-direction from Table 3) to the single direction magnetic field properties (i.e., z-direction and x-direction from Table 2). This result indicated that the porosity and pore area does not generally change as a result of applying 7.8 mT in the x- and z-direction regardless of how the field was applied (i.e., either consistently or by changing the field during freezing).

The lamellar wall data and representative SEM images in the x-z plane for the top and bottom half of these scaffolds are shown in Fig. 9. For the top half, when applying a magnetic field in the z-direction, 48% of the lamellar walls aligned in the  $90^\circ \pm 22.5^\circ$  range of angles (Fig. 9a). The representative SEM image in Fig. 9b shows this z-direction alignment. For the bottom half, when applying a magnetic field in the x-direction, 69% of the lamellar walls aligned in the  $90^\circ \pm 22.5^\circ$  range of angles (Fig. 9c). The representative SEM image in Fig. 9d shows this x-direction alignment. For the top half, there was a statistically significant difference between the  $90^\circ \pm 22.5^\circ$  range of angles and all the others, and for the bottom half, there was a statistically significant difference between the  $0^\circ \pm 22.5^\circ$  range of angles and all the others. This indicates that the lamellar walls align in the direction of the magnetic field even when it changes directions halfway through the slurry freezing.

As expected, there were no statistically significant differences in the lamellar wall directions measured in the x-y plane (Fig. 4c) between the top half (z-direction) and bottom half of the scaffold (x-direction). When imaging the location of the transition of the x-direction to the z-direction magnetic field about halfway up the scaffold, there was a clear transition. However, there was no observable gradient in lamellar wall direction between the top and bottom half of the scaffold. This suggests that the setup was able to change the magnetic field within microseconds [55] and the

**Table 3**  
The structural properties, reported as a mean  $\pm$  one standard deviation of  $n \approx 8000$  measurements of scaffolds fabricated while applying 7.8 mT at the bottom half then the top half of the scaffolds in the x-direction (x) and z-direction (z) respectively. All observed properties found to have statistically significant differences ( $\alpha = 0.05$ ) are noted by the letter a.

Magnetic Field Direction	Area Porosity (%)	Pore Area ( $\mu\text{m}^2$ )	Major Axis ( $\mu\text{m}$ )	Minor Axis ( $\mu\text{m}$ )	Pore Aspect Ratio
z (top $\frac{1}{2}$ )	20.4 $\pm$ 2.0	365 $\pm$ 214	38.5 $\pm$ 15.3	12.2 $\pm$ 3.7 <sub>a</sub>	3.5 $\pm$ 1.8
x (bottom $\frac{1}{2}$ )	21.1 $\pm$ 1.7	339 $\pm$ 161	37.5 $\pm$ 14.6	11.8 $\pm$ 3.2 <sub>a</sub>	3.5 $\pm$ 1.8

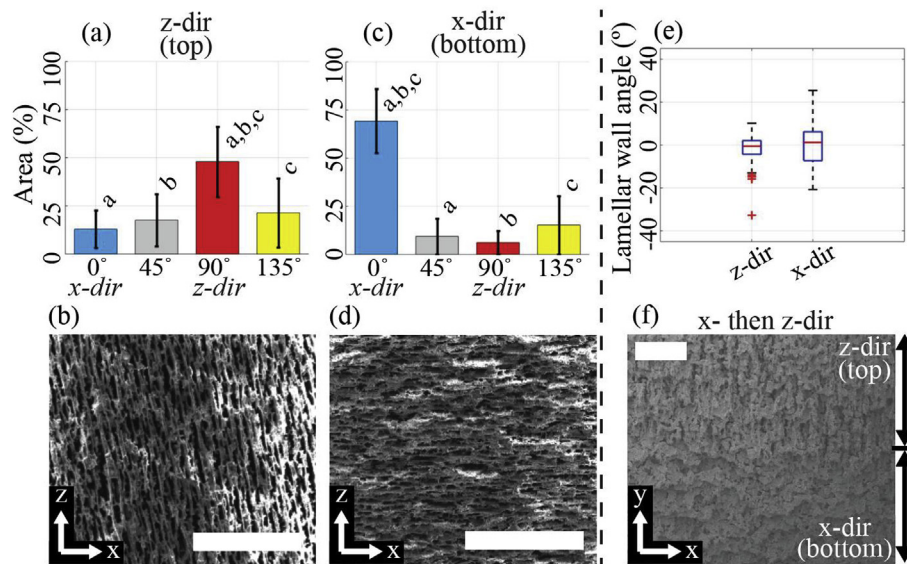


**Fig. 9.** The percent area in angle ranges  $0^\circ \pm 22.5^\circ$ ,  $45^\circ \pm 22.5^\circ$ ,  $90^\circ \pm 22.5^\circ$ , and  $135^\circ \pm 22.5^\circ$  and a representative SEM image to observe the lamellar wall directions when applying 7.8 mT in the (a, b) z-direction at the top half of the scaffolds and (c, d) x-direction at the bottom half of the scaffold. (e) A box-and-whisker plot of the measured lamellar wall directions in the x-y plane for the multi-direction magnetic field experiment and (f) a representative x-y plane SEM image of the location where the magnetic field flips from the x- to the z-direction. The '+' in the box d-and-whisker plot are outlier points. All observed properties found to have statistically significant differences ( $\alpha = 0.05$ ) are noted by matching letters a-c. The scale bars are all 200  $\mu\text{m}$ .

magnetic field's influence over the scaffold was asserted at a similarly high speed. An SEM image of this location of transition is shown in Fig. 9f where on the bottom half of the image, the magnetic field was in the x-direction and on the top half, the magnetic field was in the z-direction. When the magnetic field was in the x-direction, the wider side of the lamellar walls are observed, and when the in the z-direction, the narrower side of the lamellar walls are observed suggesting the lamellar walls are aligning in the direction of the magnetic field.

### 3.6. Multi-direction magnetic field mechanical properties

The  $\text{UCS}_x$  and  $E_x$  showed an increase of 67% and 145% from the z-direction (i.e. top) to the x-direction (i.e. bottom), respectively (Fig. 10a and b). However, only the difference in the  $E_x$  was statistically significant. This statistical difference was expected again due to the majority of the alignment of the lamellar walls being perpendicular (Fig. 9a) parallel (Fig. 9c) to the compression direction, therefore, delaying lamellar buckling.

When compressing these scaffolds in the y-direction, no statistically significant difference was expected and seen in Fig. 10c and d. This was because when compressing in the y-direction (i.e., x-z plane) if the lamellar wall direction was only rotating about the y-direction (i.e., from the x-to the z-direction), all the structural changes are occurring perpendicular to the compression direction. There was no statistically significant change in the measured pore area, and therefore, buckling and failure occur at about the same stress.

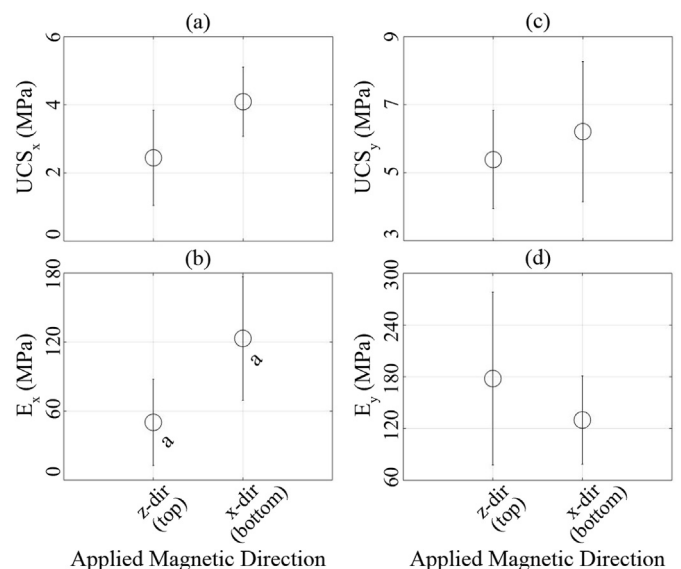


**Fig. 10.** The (a)  $\text{UCS}_x$ , (b)  $E_x$ , (c)  $\text{UCS}_y$ , and (d)  $E_y$  of scaffolds fabricated when changing the 7.8 mT magnetic field direction halfway from the freezing of the slurry from the x- to the z-direction. The values shown are the means  $\pm$  one standard deviation. All observed properties found to have statistically significant differences ( $\alpha = 0.05$ ) are noted by matching letters a.

### 3.7. Discussion

The use of a uniform magnetic field has been shown to alter the structural and mechanical characteristics through the alignment of particles. This additional magnetic force alters the freezing dynamics to create various sizes and shapes of pores, furthering the capabilities to customize the properties of freeze-cast scaffolds. Because of this ability to customize the structural properties, the number of possible applications increases.

These results extend the ways that freeze-cast scaffolds can be customized to have user-specific properties through the implementation of a uniform magnetic field to manipulate particles and by changing the magnetic field direction at any time. This customization of the structural and mechanical properties can lead to advancements in a variety of engineering applications. Materials other than  $\text{Fe}_3\text{O}_4$  could potentially be used in this magnetic freeze-casting process such as  $\text{ZrO}_2$  [36] for biomedical applications or structural composites,  $\text{Al}_2\text{O}_3$  [37] for insulators, or metals [15,61] for supercapacitors.

For materials with lower magnetization, a higher uniform magnetic field might be required to manipulate and align particles in the ways seen here. Increasing the magnetic properties of paramagnetic or diamagnetic particles through processes such as surface-magnetization could be used to achieve particle manipulation [24,62].

Besides the size limit of commercially available materials, there are no limitations to the size that one can build a Helmholtz coil and freeze-cast setup. So this setup could, in theory, be scaled up and further customized to produce scaffolds of different shapes and sizes. However, it should be noted that this would require large solenoids that would employ very high currents. This could result in physical complications in terms of power generation and energy costs, and potentially dangerous conditions.

Although the magnetic field is much lower using tri-axial nested Helmholtz coils, the increase in mechanical properties was up to 308% compared to previous permanent magnet freeze-casting setups where increases of only up to 100% were observed [37,38]. This is likely due to more lamellar walls aligning in the compression direction from the uniform magnetic field generated from the Helmholtz coils (up to 81%) compared to previous reported alignment of approximately 20% [37]. Also, due to the uniform magnetic field, particle agglomeration has been effectively eliminated from the current setup, while particle agglomeration was observed in previous permanent magnetic freeze casting experiments [36,38,40], which can further contribute to the results.

Due to the sintering process, the particles became weakly ferromagnetic which would be critical if integrating the scaffolds in an application where low magnetic properties are desired. If the desire is to keep the higher magnetic properties, altering the sintering process by sintering in an inert Argon gas environment is one way that can be done [52].

### 4. Conclusions

This investigation into altering the magnetic field direction during freeze casting using  $\text{Fe}_3\text{O}_4$  slurries leads to the following conclusions:

- Lamellar wall alignment was achieved through the various applied magnetic field directions expanding on the ability to customize the structural and mechanical properties of porous scaffolds through the freeze-casting process.
- Using ferrimagnetic particles to create weakly ferromagnetic scaffolds was achieved with the sintering process.

- The tri-axial nested Helmholtz coils aligned  $\text{Fe}_3\text{O}_4$  particles in every magnetic field direction applied in this research. Of specific note, 80% and 81% of walls aligned with a magnetic field applied in the x- and z-direction, respectively.
- The pore area, major axis, minor axis, and pore aspect ratio increased when applying a magnetic field transverse to the ice growth direction (i.e., x- and z-direction) due to the particles being rejected by the freezing front.
- The  $\text{UCS}_x$  and  $E_x$  increased by 142% and 73% and 308% and 205% when applying a magnetic field in the x- and 45°-direction, respectively when compared to no applied field, due to the lamellar walls aligning in the x-direction.
- When changing the magnetic field direction from the x- to the z-direction halfway through the freezing the slurry, the lamellar walls changed directions to align with the magnetic field.
- This novel tri-axial nested Helmholtz coils setup was able to provide greater control over magnetic freeze casting than previous magnetic freeze-casting experimental setups.

### Acknowledgments

This work was financially supported in part by the National Science Foundation under grant CMMI #1660979. The authors would like to thank Advanced Motion Control for generous academic discounts on the servo drives used to control the tri-axial nested Helmholtz coils.

### References

- [1] S.W. Sofie, F. Dogan, Freeze casting of aqueous alumina slurries with glycerol, *J. Am. Ceram. Soc.* 84 (7) (2001) 1459–1464.
- [2] K. Araki, J.W. Halloran, Porous ceramic bodies with interconnected pore channels by a novel freeze casting technique, *J. Am. Ceram. Soc.* 88 (5) (2005) 1108–1114.
- [3] S. Deville, E. Saiz, R.K. Nalla, A.P. Tomsia, Freezing as a path to build complex composites, *Science* 311 (515) (2006) 8.
- [4] S. Deville, E. Saiz, A.P. Tomsia, Ice-templated porous alumina structures, *Acta Mater.* 55 (6) (2007) 1965–1974.
- [5] S. Deville, Freeze-casting of porous ceramics: a review of current achievements and issues, *Adv. Eng. Mater.* 10 (3) (2008) 155–169.
- [6] S. Deville, E. Saiz, A.P. Tomsia, Freeze casting of hydroxyapatite scaffolds for bone tissue engineering, *Biomaterials* 27 (32) (2006) 5480–5489.
- [7] E. Munch, J. Franco, S. Deville, P. Hunger, E. Saiz, A.P. Tomsia, Porous Ceramic Scaffolds with Complex Architectures, Lawrence Berkeley National Laboratory, 2008.
- [8] T.A. Ogden, M. Prisbrey, I. Nelson, B. Raeymaekers, S.E. Naleway, Bioinspired ultrasound freeze casting: engineered porous scaffolds through freeze casting and ultrasound directed self-assembly, *Mater. Des.* 164 (2018).
- [9] H.W. Kang, Y. Tabata, Y. Ikada, Fabrication of porous gelatin scaffolds for tissue engineering, *Biomaterials* 20 (14) (1999) 1339–1344.
- [10] H. Schoof, J. Apel, I. Heschel, G. Rau, Control of pore structure and size in freeze-dried collagen sponges, *J. Biomed. Mater. Res.* 58 (4) (2001) 352–357.
- [11] M.V. Dinu, M. Pradny, E.S. Dragan, J. Michalek, Ice-templated hydrogels based on chitosan with tailored porous morphology, *Carbohydr. Polym.* 94 (1) (2013) 170–178.
- [12] N.L. Francis, P.M. Hunger, A.E. Donius, B.W. Riblett, A. Zavaliangos, U.G. Wegst, M.A. Wheatley, An ice-templated, linearly aligned chitosan-alginate scaffold for neural tissue engineering, *J. Biomed. Mater. Res. A* 101 (12) (2013) 3493–3503.
- [13] T. Kohnke, T. Elder, H. Theliander, A.J. Ragauskas, Ice templated and cross-linked xylan/nanocrystalline cellulose hydrogels, *Carbohydr. Polym.* 100 (2014) 24–30.
- [14] H.-D. Jung, S.-W. Yook, H.-E. Kim, Y.-H. Koh, Fabrication of titanium scaffolds with porosity and pore size gradients by sequential freeze casting, *Mater. Lett.* 63 (17) (2009) 1545–1547.
- [15] H.D. Jung, S.W. Yook, T.S. Jang, Y. Li, H.E. Kim, Y.H. Koh, Dynamic freeze casting for the production of porous titanium (Ti) scaffolds, *Mater Sci Eng C Mater Biol Appl* 33 (1) (2013) 59–63.
- [16] Y. Chino, D.C. Dunand, Directionally freeze-cast titanium foam with aligned, elongated pores, *Acta Mater.* 56 (1) (2008) 105–113.
- [17] J.C. Li, D.C. Dunand, Mechanical properties of directionally freeze-cast titanium foams, *Acta Mater.* 59 (1) (2011) 146–158.
- [18] S.E. Naleway, C.F. Yu, M.M. Porter, A. Sengupta, P.M. Iovine, M.A. Meyers, J. McKittrick, Bioinspired composites from freeze casting with clathrate hydrates, *Mater. Des.* 71 (2015) 62–67.
- [19] S. Roy, A. Wanner, Metal/ceramic composites from freeze-cast ceramic

- preforms: domain structure and elastic properties, *Compos. Sci. Technol.* 68 (5) (2008) 1136–1143.
- [20] E. Munch, E. Saiz, A.P. Tomsia, S. Deville, Architectural control of freeze-cast ceramics through additives and templating, *J. Am. Ceram. Soc.* 92 (7) (2009) 1534–1539.
- [21] S.E. Naleway, K.C. Fickas, Y.N. Maker, M.A. Meyers, J. McKittrick, Reproducibility of ZrO<sub>2</sub>-based freeze casting for biomaterials, *Mater Sci Eng C Mater Biol Appl* 61 (2016) 105–112.
- [22] S.W. Sofie, Fabrication of functionally graded and aligned porosity in thin ceramic substrates with the novel freeze-tape-casting process, *J. Am. Ceram. Soc.* 90 (7) (2007) 2024–2031.
- [23] L. Qian, H. Zhang, Controlled freezing and freeze drying: a versatile route for porous and micro-/nano-structured materials, *J. Chem. Technol. Biotechnol.* 86 (2) (2011) 172–184.
- [24] M.B. Frank, S. Hei Siu, K. Karandikar, C.H. Liu, S.E. Naleway, M.M. Porter, O.A. Graeve, J. McKittrick, Synergistic structures from magnetic freeze casting with surface magnetized alumina particles and platelets, *J. Mech. Behav. Biomed. Mater.* 76 (2017) 153–163.
- [25] P.M. Hunger, A.E. Donius, U.G. Wegst, Platelets self-assemble into porous nacre during freeze casting, *J. Mech. Behav. Biomed. Mater.* 19 (2013) 87–93.
- [26] S. Deville, E. Maire, A. Lasalle, A. Bogner, C. Gauthier, J. Leloup, C. Guizard, In situ X-ray radiography and tomography observations of the solidification of aqueous alumina particle suspensions-Part I: initial instants, *J. Am. Ceram. Soc.* 92 (11) (2009) 2489–2496.
- [27] S. Deville, E. Maire, G. Bernard-Granger, A. Lasalle, A. Bogner, C. Gauthier, J. Leloup, C. Guizard, Metastable and unstable cellular solidification of colloidal suspensions, *Nat. Mater.* 8 (12) (2009) 966–972.
- [28] P.M. Hunger, A.E. Donius, U.G. Wegst, Structure-property-processing correlations in freeze-cast composite scaffolds, *Acta Biomater.* 9 (5) (2013) 6338–6348.
- [29] A. Preiss, B. Su, S. Collins, D. Simpson, Tailored graded pore structure in zirconia toughened alumina ceramics using double-side cooling freeze casting, *J. Eur. Ceram. Soc.* 32 (8) (2012) 1575–1583.
- [30] H. Bai, Y. Chen, B. Delattre, A.P. Tomsia, R.O. Ritchie, Bioinspired large-scale aligned porous materials assembled with dual temperature gradients, *Sci. Adv.* 1 (11) (2015) e1500849–e1500849.
- [31] H. Bai, F. Walsh, B. Gludovatz, B. Delattre, C. Huang, Y. Chen, A.P. Tomsia, R.O. Ritchie, Bioinspired hydroxyapatite/poly(methyl methacrylate) composite with a nacre-mimetic architecture by a bidirectional freezing method, *Adv. Mater.* 28 (1) (2016) 50–56.
- [32] J.-W. Moon, H.-J. Hwang, M. Awano, K. Maeda, Preparation of NiO–YSZ tubular support with radially aligned pore channels, *Mater. Lett.* 57 (8) (2003) 1428–1434.
- [33] Y. Tang, Q. Miao, S. Qiu, K. Zhao, L. Hu, Novel freeze-casting fabrication of aligned lamellar porous alumina with a centrosymmetric structure, *J. Eur. Ceram. Soc.* 34 (15) (2014) 4077–4082.
- [34] H. Bai, D. Wang, B. Delattre, W. Gao, J. De Coninck, S. Li, A.P. Tomsia, Bio-mimetic gradient scaffold from ice-templating for self-seeding of cells with capillary effect, *Acta Biomater.* 20 (2015) 113–119.
- [35] Y. Tang, S. Qiu, Q. Miao, C. Wu, Fabrication of lamellar porous alumina with axisymmetric structure by directional solidification with applied electric and magnetic fields, *J. Eur. Ceram. Soc.* 36 (5) (2016) 1233–1240.
- [36] M.M. Porter, L. Meraz, A. Calderon, H. Choi, A. Chouhan, L. Wang, M.A. Meyers, J. McKittrick, Torsional properties of helix-reinforced composites fabricated by magnetic freeze casting, *Compos. Struct.* 119 (2015) 174–184.
- [37] M.B. Frank, S.E. Naleway, T. Haroush, C.-H. Liu, S.H. Siu, J. Ng, I. Torres, A. Ismail, K. Karandikar, M.M. Porter, O.A. Graeve, J. McKittrick, Stiff, porous scaffolds from magnetized alumina particles aligned by magnetic freeze casting, *Mater. Sci. Eng. C* 77 (2017) 484–492.
- [38] M.M. Porter, M. Yeh, J. Strawson, T. Goehring, S. Lujan, P. Siripapasotorn, M.A. Meyers, J. McKittrick, Magnetic freeze casting inspired by nature, *Mater. Sci. Eng., A* 556 (2012) 741–750.
- [39] I. Nelson, T.A. Ogden, S. Al Khateeb, J. Graser, T.D. Sparks, J.J. Abbott, S.E. Naleway, Freeze-Casting of Surface-Magnetized Iron(II,III) Oxide Particles in a Uniform Static Magnetic Field Generated by a Helmholtz Coil, *Advanced Engineering Materials* in Press, 2019.
- [40] M.M. Porter, P. Niksiar, J. McKittrick, G. Franks, Microstructural control of colloidal-based ceramics by directional solidification under weak magnetic fields, *J. Am. Ceram. Soc.* 99 (6) (2016) 1917–1926.
- [41] I. Nelson, S.E. Naleway, Intrinsic and extrinsic control of freeze casting, *J. Mater. Res. Technol.* (2019) in press.
- [42] L. Ren, Y.-P. Zeng, D. Jiang, Preparation of porous TiO<sub>2</sub> by a novel freeze casting, *Ceram. Int.* 35 (3) (2009) 1267–1270.
- [43] H. Yoshikawa, A. Myoui, Bone tissue engineering with porous hydroxyapatite ceramics, *J. Artif. Organs* 8 (3) (2005) 131–136.
- [44] Y. Tang, K. Zhao, L. Hu, Z. Wu, Two-step freeze casting fabrication of hydroxyapatite porous scaffolds with bionic bone graded structure, *Ceram. Int.* 39 (8) (2013) 9703–9707.
- [45] E.-J. Lee, Y.-H. Koh, B.-H. Yoon, H.-E. Kim, H.-W. Kim, Highly porous hydroxyapatite bioceramics with interconnected pore channels using camphene-based freeze casting, *Mater. Lett.* 61 (11–12) (2007) 2270–2273.
- [46] G. Wei, P.X. Ma, Structure and properties of nano-hydroxyapatite/polymer composite scaffolds for bone tissue engineering, *Biomaterials* 25 (19) (2004) 4749–4757.
- [47] S.E. Naleway, C.F. Yu, R.L. Hsiong, A. Sengupta, P.M. Iovine, J.A. Hildebrand, M.A. Meyers, J. McKittrick, Bioinspired intrinsic control of freeze cast composites: harnessing hydrophobic hydration and clathrate hydrates, *Acta Mater.* 114 (2016) 67–79.
- [48] M.E. Launey, E. Munch, D.H. Alsem, E. Saiz, A.P. Tomsia, R.O. Ritchie, A novel biomimetic approach to the design of high-performance ceramic-metal composites, *J. R. Soc. Interface* 7 (46) (2010) 741–753.
- [49] J.J. Abbott, Parametric design of tri-axial nested Helmholtz coils, *Rev. Sci. Instrum.* 86 (054701) (2015) 10.
- [50] A.M.A. Silva, E.H.M. Nunes, D.F. Souza, D.L. Martens, J.C. Diniz da Costa, M. Houmar, W.L. Vasconcelos, Effect of titania addition on the properties of freeze-cast alumina samples, *Ceram. Int.* 41 (9) (2015) 10467–10475.
- [51] D.F. Souza, E.H.M. Nunes, D.S. Pimenta, D.C.L. Vasconcelos, J.F. Nascimento, W. Grava, M. Houmar, W.L. Vasconcelos, Synthesis and structural evaluation of freeze-cast porous alumina, *Mater. Char.* 96 (2014) 183–195.
- [52] T.K. Sandeep Kumar, Investigation of Sintering Kinetics of Magnetite Pellets during Induration, Department of Civil, Environmental and Natural Resources Engineering, Luleå University of Technology, 2015, p. 85.
- [53] S. Deville, Ice-templating, freeze casting: beyond materials processing, *J. Mater. Res.* 28 (17) (2013) 2202–2219.
- [54] S. Deville, E. Maire, A. Lasalle, A. Bogner, C. Gauthier, J. Leloup, C. Guizard, Influence of particle size on ice nucleation and growth during the ice-templating process, *J. Am. Ceram. Soc.* 93 (9) (2010) 2507–2510.
- [55] N. Instrument, Datasheet NI 9263, 2015.
- [56] N.N. Greenwood, A. Earnshaw, *Chemistry of the Elements*, second ed., Reed Educational and Professional Publishing Ltd 1984, Oxford, England, 1997.
- [57] B.E. Monsen, S.E. Olsen, L. Kolbeinsen, Kinetics of magnetite oxidation, *Scand. J. Metall.* 23 (2) (1994) 74–80.
- [58] E.R. Monazam, R.W. Breault, R.V. Siriwardane, Kinetics of magnetite (Fe<sub>3</sub>O<sub>4</sub>) oxidation to hematite (Fe<sub>2</sub>O<sub>3</sub>) in air for chemical looping combustion, *Ind. Eng. Chem. Res.* 53 (2014) 13320–13328.
- [59] D.R. Gaskell, *Introduction to the Thermodynamics of Material*, fourth ed., Taylor & Francis Books Inc, New York City, NY, USA, 2003.
- [60] M.M. Porter, R. Imperio, M. Wen, M.A. Meyers, J. McKittrick, Bioinspired scaffolds with varying pore architectures and mechanical properties, *Adv. Funct. Mater.* 24 (14) (2014) 1978–1987.
- [61] A. Shaga, P. Shen, C. Sun, Q. Jiang, Lamellar-interpenetrated Al–Si–Mg/SiC composites fabricated by freeze casting and pressureless infiltration, *Mater. Sci. Eng., A* 630 (2015) 78–84.
- [62] R.M. Erb, R. Libanori, N. Rothfuchs, A.R. Studart, Composites reinforced in three dimensions by using low magnetic fields, *Science* 335 (6065) (2012) 199–204.